

Luminescence and Energy Transfer between Ce³⁺ and Pr³⁺ in BaY₂Si₃O₁₀ under VUV-vis and X-ray Excitation

Shi, Rui; Huang, Yan; Tao, Ye; Dorenbos, Pieter; Ni, Haiyong; Liang, Hongbin

DOI

[10.1021/acs.inorgchem.8b01084](https://doi.org/10.1021/acs.inorgchem.8b01084)

Publication date

2018

Document Version

Final published version

Published in

Inorganic Chemistry

Citation (APA)

Shi, R., Huang, Y., Tao, Y., Dorenbos, P., Ni, H., & Liang, H. (2018). Luminescence and Energy Transfer between Ce³⁺ and Pr³⁺ in BaY₂Si₃O₁₀ under VUV-vis and X-ray Excitation. *Inorganic Chemistry*, 57(14), 8414-8421. <https://doi.org/10.1021/acs.inorgchem.8b01084>

Important note

To cite this publication, please use the final published version (if applicable). Please check the document version above.

Copyright

Other than for strictly personal use, it is not permitted to download, forward or distribute the text or part of it, without the consent of the author(s) and/or copyright holder(s), unless the work is under an open content license such as Creative Commons.

Takedown policy

Please contact us and provide details if you believe this document breaches copyrights. We will remove access to the work immediately and investigate your claim.

Luminescence and Energy Transfer between Ce³⁺ and Pr³⁺ in BaY₂Si₃O₁₀ under VUV–vis and X-ray Excitation

Rui Shi,[†] Yan Huang,[‡] Ye Tao,[‡] Pieter Dorenbos,[§] Haiyong Ni,^{||} and Hongbin Liang^{*,†}

[†]MOE Laboratory of Bioinorganic and Synthetic Chemistry, KLGHEI of Environment and Energy Chemistry, School of Chemistry, Sun Yat-sen University, Guangzhou 510275, China

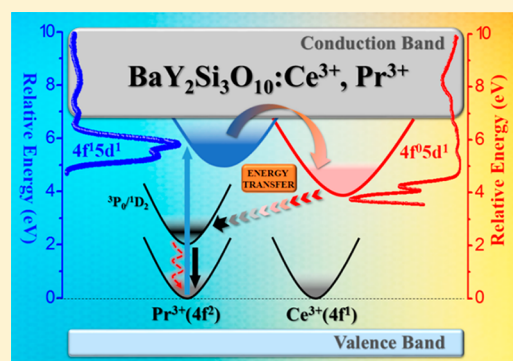
[‡]Beijing Synchrotron Radiation Facility, Institute of High Energy Physics, Chinese Academy of Sciences, Beijing 100039, China

[§]Faculty of Applied Sciences, Delft University of Technology, Mekelweg 15, 2629 JB Delft, The Netherlands

^{||}Guangdong Research Institute of Rare Metals, Guangzhou 510650, China

Supporting Information

ABSTRACT: A detailed investigation on photoluminescence properties and energy transfer (ET) dynamics of Ce³⁺, Pr³⁺-doped BaY₂Si₃O₁₀ is provided along with the potential X-ray excited luminescence application. The luminescence properties of Pr³⁺ are studied in VUV–UV–vis spectral range at low temperature, and the spectral profiles of Pr³⁺ ³P₀ and ¹D₂ emission lines are determined using time-resolved emission spectra. Upon 230 nm excitation, the electron population from Pr³⁺ 4f5d state to its 4f² excited state is discussed in detail. As Pr³⁺ concentration rises, Pr³⁺ ³P₀ and ¹D₂ luminescence possess different concentration-related properties. The incorporation of Ce³⁺ in the codoped sample produces the strong Ce³⁺ luminescence under 230 nm excitation, which is the combined result of Pr³⁺ 4f5d → Ce³⁺ 5d ET and Ce³⁺ intrinsic excitation. On the other hand, the increasingly strong ET of Ce³⁺ 5d → Pr³⁺ 4f² results in the decrease of Ce³⁺ emission intensity and the gradual deviation of Ce³⁺ luminescence decay from the single exponential in the system. By employing the Inokuti–Hirayama model, the dipole–dipole interaction is confirmed as the predominant multipolar effect in controlling this ET process, and the value of C_{DA} is determined to be 9.97 × 10^{−47} m⁶·s^{−1}. Finally, the relatively low scintillation light yield of Ce³⁺-doped BaY₂Si₃O₁₀ material impedes its application potential in the scintillator field, and the cosubstitution of Pr³⁺ results in the observable decline of scintillation performance.



INTRODUCTION

Pr³⁺ is a lanthanide ion with 4f² electron configuration. It is an important activator in luminescent materials for applications in lighting, display, detecting, thermometry, and so on. For example, the red-emitting β-SiAlON:Pr³⁺ phosphor with high thermal stability is a good candidate for light emitting diodes (LEDs).¹ The phosphor SrTiO₃:Pr³⁺ shows the fast optical response; therefore, it has been recommended to be used in color field emission displays (FEDs). The ceramic Gd₂O₂S:Pr³⁺-Ce³⁺ is a commercially available scintillator for detecting in X-ray computed tomography (X-CT).² Recently, we reported the thermometric property of Pr³⁺ in La₂MgTiO₆.³ All these applications derive from the host compound dependent on the electronic transitions of Pr³⁺. To find new luminescent materials, it is essential to clearly understand the various electronic transitions of Pr³⁺ in different host compounds.

The energy transfer (ET) has always been a crucial topic of luminescent materials. For Ce³⁺ and Pr³⁺ codoped systems, most literature only deals with the ET from 5d states of Ce³⁺ to 4f² states of Pr³⁺, but the ET between 5d states of Pr³⁺ and Ce³⁺ is seldom studied.^{4,5} This may relate to the high energies

of Pr³⁺ 4f5d states in the vacuum ultraviolet (VUV, wavelength λ < 200 nm) region in most fluorides and complex oxides and the lack of experimental equipment in this region. When Ce³⁺ and Pr³⁺ ions replace sites of the same type of a given host compound, Pr³⁺ 4f²-4f5d transition energies are usually higher than those of Ce³⁺; therefore, the ET from the Pr³⁺ 4f5d state to the Ce³⁺ 5d state is possible. Whether this type of ET process occurs depends on the spectral overlapping between Pr³⁺ f-d emission and Ce³⁺ f-d excitation bands. So, it is necessary to precisely determine the 5d energies in the VUV–UV region, to fully understand the ET between Ce³⁺ and Pr³⁺.

In this article we study the VUV–UV–vis luminescence properties of Pr³⁺ in BaY₂Si₃O₁₀ by employing the synchrotron radiation facility. The time-resolved emission spectra (TRES) are used to determine the Pr³⁺ ³P₀ and ¹D₂ emission lines, and concentration-dependent luminescence of Pr³⁺ f-d/f-f transitions are systemically investigated. We focus on the understanding of 5d energies of Pr³⁺ in BaY₂Si₃O₁₀ and the ET between Ce³⁺ and Pr³⁺, especially the ET from Pr³⁺ 4f5d

Received: April 19, 2018

Published: June 26, 2018

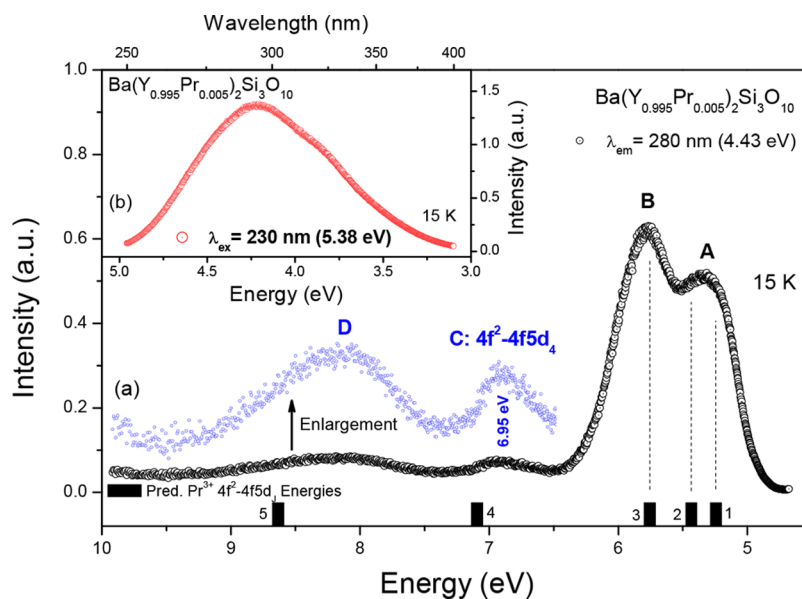


Figure 1. (a) VUV–UV excitation spectrum of $\text{Ba}(\text{Y}_{0.995}\text{Pr}_{0.005})_2\text{Si}_3\text{O}_{10}$ with 280 nm (4.43 eV) emission at 15 K; (b) emission spectrum under 230 nm (5.38 eV) excitation.

state to Ce^{3+} 5d state in this compound. Finally, the X-ray excitation luminescence (XEL) performances of Ce^{3+} , Pr^{3+} -doped materials are conducted.

SAMPLES PREPARATION AND MEASUREMENTS

Several series of Ce^{3+} , Pr^{3+} -doped/codoped $\text{BaY}_2\text{Si}_3\text{O}_{10}$ samples were prepared by a high temperature solid-state reaction technique. The detailed information on sample preparation and measurement are given in the Supporting Information (SI).

RESULTS AND DISCUSSIONS

Structure Characteristic. $\text{BaY}_2\text{Si}_3\text{O}_{10}$, with the monoclinic structure, possesses only one kind of lanthanide (Ln^{3+})-substitutable Y^{3+} site with 6-fold coordination.⁶ Herein, X-ray diffraction (XRD) patterns of representative samples at room temperature (RT) are displayed in Figure S1. No significant second phase can be detected, and all patterns are in accord with the standard pattern, indicating that the dopant Ce^{3+} and Pr^{3+} ions occupy Y^{3+} sites and this substitution has little influence on the crystal structure of studied compounds.

Luminescence of Pr^{3+} in $\text{Ba}(\text{Y}_{1-x}\text{Pr}_x)_2\text{Si}_3\text{O}_{10}$. Figure 1a gives the VUV–UV excitation spectrum of $\text{Ba}(\text{Y}_{0.995}\text{Pr}_{0.005})_2\text{Si}_3\text{O}_{10}$ with 280 nm (4.43 eV) emission at 15 K. Two intense excitation bands [A (5.35 eV) and B (5.78 eV)] in the low-energy region (<6.5 eV) and a weak excitation C with the maximum at 6.95 eV are observed. Besides, a broad absorption D can be detected in the high-energy region (>7.5 eV). These bands are attributed to the $4f^2-4f5d$ transitions of Pr^{3+} and the host-related absorption. Five main 4f5d bands are expected to occur in the excitation spectrum of Pr^{3+} in the Y^{3+} site of $\text{BaY}_2\text{Si}_3\text{O}_{10}$ to a first approximation, but the f–d transitions of Pr^{3+} are actually a little complicated in comparison with those of Ce^{3+} . This is because the interactions between the 4f electron and the 5d electron in the Pr^{3+} ion will give rise to many fd energy levels in addition to vibronic lines.⁷ As a rough estimation, we just discuss the energies of the main bands. Because of the approximate crystal field strength and nephelauxetic effect of different Ln^{3+} ions in sites of the

same type of a given host compound,⁸ the 4f5d energy splitting of Pr^{3+} is generally consistent with that of Ce^{3+} in $\text{BaY}_2\text{Si}_3\text{O}_{10}$ at first glance. Two intense bands are observed above 250 nm in the excitation spectrum of $\text{Ba}(\text{Y}_{0.99}\text{Ce}_{0.01})_2\text{Si}_3\text{O}_{10}$ as displayed in Figure S2, which actually contain three excitation bands and can be assigned to electronic transitions from the Ce^{3+} 4f ground state to its first ($5d_1$), second ($5d_2$), and third ($5d_3$) 5d excited states (denoted as $4f-5d_{1-3}$ transitions).^{6,9–11} Accordingly, bands A and B in Figure 1a should be attributed to the superposition of Pr^{3+} $4f^2-4f5d_{1-3}$ transitions. To estimate the energies of Pr^{3+} $4f^2-4f5d_{1-5}$ transitions, the $4f-5d_j$ ($J = 1, 2, 3, 4, 5$) transitions of Ce^{3+} are shifted toward the high-energy direction about 1.51 eV, considering the energy difference between the lowest 5d states of free Ce^{3+} (6.12 eV) and Pr^{3+} (7.63 eV).¹² The predicated five $4f^2-4f5d_{1-5}$ transition energies of Pr^{3+} are plotted as black bars in Figure 1, which show that the predicated Pr^{3+} $4f^2-4f5d_{1-3}$ energies are in accord with the experimental findings, confirming the attributions of excitation bands given above. Because of the overlap to host-related absorption, the $4f^2-4f5d_{4,5}$ transitions of Pr^{3+} are not observed in the spectrum.

Under 230 nm (5.38 eV) excitation, the sample shows a broad emission band from 250 to 400 nm as displayed in Figure 1b, corresponding to Pr^{3+} $4f5d_{1-3}H_{4-6}$ parity-allowed emissions. Given that the energy differences between adjacent 3H_J ($J = 4, 5, 6$) states of Pr^{3+} are about 2000 cm^{-1} (0.25 eV) and given the significant coupling of the Pr^{3+} 4f5d orbit with the surrounding coordination environment, multiple emission progressions are obscured in the spectrum. Figure S3 presents Pr^{3+} f–d luminescence decay in $\text{Ba}(\text{Y}_{0.995}\text{Pr}_{0.005})_2\text{Si}_3\text{O}_{10}$ at RT. The decay signal of the sample is somewhat blurred by the impulse response function (IRF) of the excitation source before 25 ns. After deconvolution of the experimental curve using IRF, the decay signal of Pr^{3+} is extracted, and the decay time is roughly estimated within the 10–15 ns region. Since the decay time shortens with the third power of the wavelength, the emission of Pr^{3+} at a shorter wavelength leads to a faster decay in comparison with that of Ce^{3+} (33.5 ns).

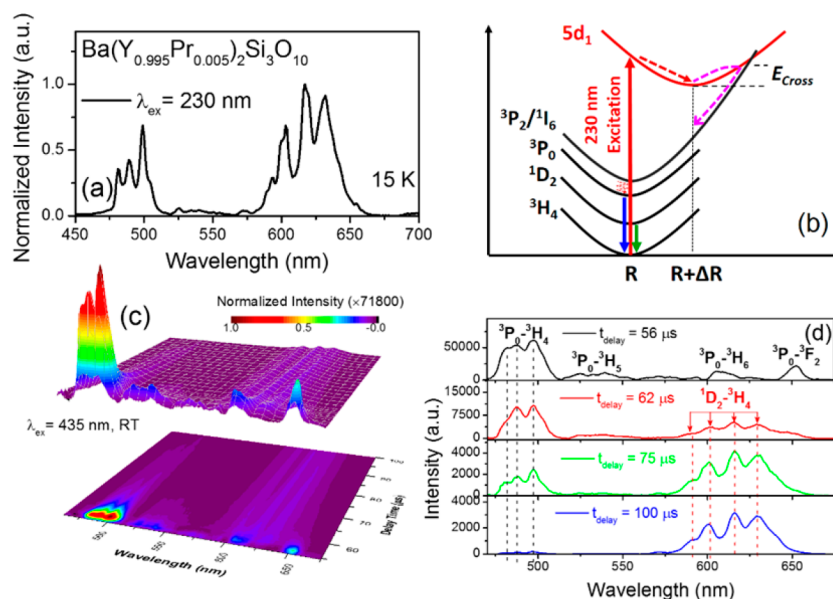


Figure 2. (a) Normalized emission spectrum of $\text{Ba}(\text{Y}_{0.995}\text{Pr}_{0.005})_2\text{Si}_3\text{O}_{10}$ under 230 nm (4.43 eV) excitation at 15 K in the 450–700 nm wavelength region; (b) the configurational coordinate diagram of Pr^{3+} and possible electron population pathway from the $4f5d_1$ state to $4f^2$ states; (c) the 3D color-filled contour of TRES of sample under 435 nm excitation at RT; (d) spectral slices of sample at different delay times.

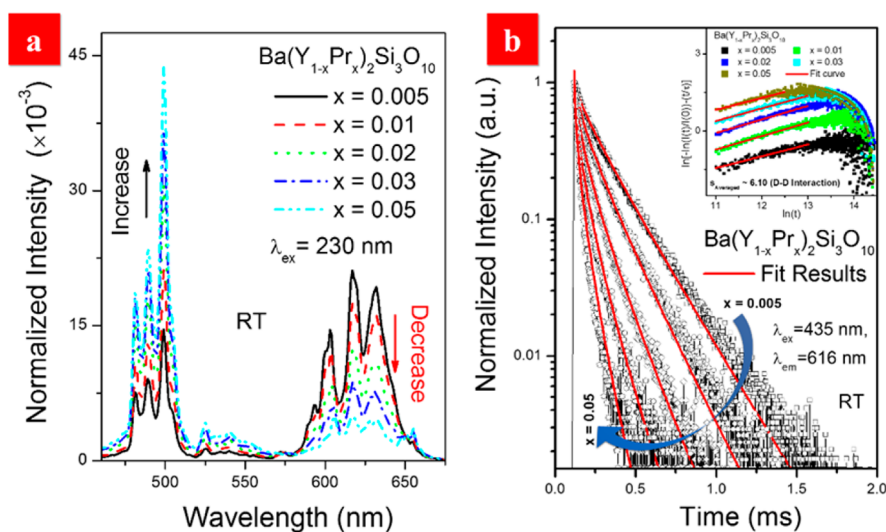


Figure 3. (a) Normalized $f-f$ emission spectra of $\text{Ba}(\text{Y}_{1-x}\text{Pr}_x)_2\text{Si}_3\text{O}_{10}$ ($x = 0.005-0.05$) under 230 nm excitation; (b) $^1\text{D}_2$ luminescence decays in samples with different concentrations at RT; the red lines denote the fitting results by the Inokuti–Hirayama model, and the inset represents the fitting results of the multipolar mechanism.

Apart from Pr^{3+} $f-d$ emissions, the sample also shows $f-f$ emissions under 230 nm excitation. As depicted in Figure 2a, these $f-f$ transitions are assigned to transitions arising from Pr^{3+} $^3\text{P}_0$ (mainly around 500 nm, the strongest line at 498 nm) and $^1\text{D}_2$ excited states (around 600 nm, the strongest line at 616 nm).^{13,14} After 230 nm excitation, the $5d$ electrons may radiatively return to the ground state by $f-d$ emissions; at the same time they can also populate the next lower-lying $4f$ excited states through the crossover pathway as shown in the configurational coordinate diagram of Figure 2b. That is to say, the $5d$ electrons can overcome the energy barrier E_{Cross} with the contribution of vibronic coupling and give rise to the population from the Pr^{3+} emitting- $4f5d_1$ state to its $4f^2$ states, and finally result in $f-f$ emissions.

Figure 2c represents the 3D color-filled contour of TRES under 435 nm $^3\text{H}_4-^3\text{P}_2$ excitation at RT, and spectral slices at

different delay times are shown in Figure 2d. Generally, the selection rule mainly controls the transition possibilities of $4f-4f$ emissions of Ln^{3+} ; therefore, the decays of $^3\text{P}_0-^3\text{H}_{4-6}$ transitions are usually faster than those of $^1\text{D}_2-^3\text{H}_{4-6}$ transitions.³ Several emission lines arising from the $^3\text{P}_0$ state are observed within the short delay time ($t_{\text{delay}} \sim 56 \mu\text{s}$), and no significant $^1\text{D}_2-^3\text{H}_4$ emission can be detected. With a gradual rise in t_{delay} to $62 \mu\text{s}$, the emission intensity of $^3\text{P}_0$ decreases and $^1\text{D}_2$ luminescence emerges out around 600 nm as marked by red arrows in the figure. Further increasing t_{delay} (to $75 \mu\text{s}$) results in a significant drop of $^3\text{P}_0$ emission, and its intensity is weaker than that of $^1\text{D}_2$. When t_{delay} increases to $100 \mu\text{s}$, $^1\text{D}_2$ emission becomes dominant and the contribution of $^3\text{P}_0$ emission is almost negligible. The results demonstrate that the electrons in the $^3\text{P}_0$ excited state may nonradiatively

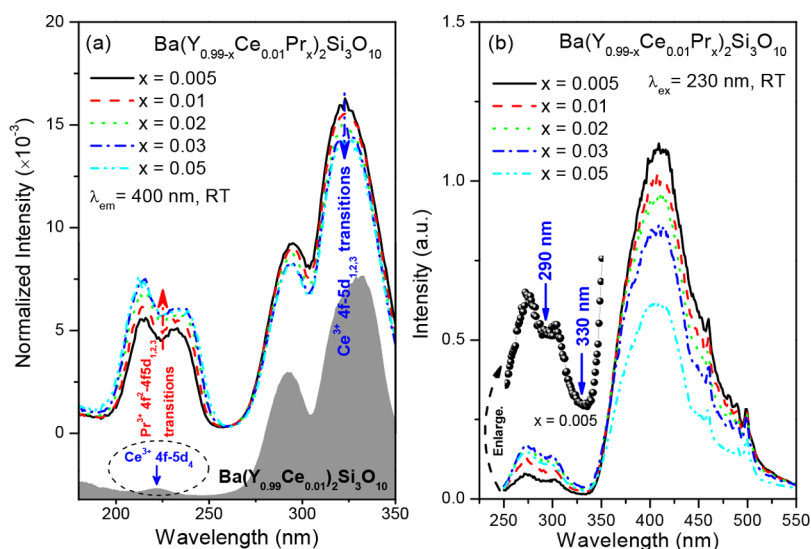


Figure 4. (a) Normalized excitation spectra of Ba(Y_{0.99-x}Ce_{0.01}Pr_x)₂Si₃O₁₀ ($x = 0.005\text{--}0.05$) samples with 400 nm Ce³⁺ f-d emission as well as the excitation spectrum of Ba(Y_{0.99}Ce_{0.01})₂Si₃O₁₀; (b) emission spectra of samples under 230 nm Pr³⁺ excitation; the inset (black dots) displays the enlargement of the spectrum ($x = 0.005$) in the 250–350 nm region.

populate the next lower-lying ¹D₂ state besides the radiative transition back to ³H_j ground states.

The population from ³P₀ to ¹D₂ states is usually through cross relaxation (CR) and multiphonon relaxation (MPR) processes. Because of the extremely low Pr³⁺ concentration in Ba(Y_{0.995}Pr_{0.005})₂Si₃O₁₀, Pr³⁺ is regarded as an isolated ion and the possible CR between different Pr³⁺ is negligible. So only MPR is considered herein, and its rate can be estimated by the modified exponential energy gap equation:¹⁵

$$W_{MPR}^{(T)} = \beta[-\alpha(\Delta E - 2h\nu)][1 - \exp(-h\nu_{max}/kT)]^{-p}$$

where constants β and α are 10⁷ s⁻¹ and 4.5(±1) × 10⁻³ cm¹⁶, ΔE is the energy gap between ³P₀ and ¹D₂ (~3450 cm⁻¹), $h\nu_{max}$ is the highest vibrational energy in the silicate lattice (~1050 cm⁻¹)¹⁷ after comparing with the energy of the Pr–O stretching vibration mode (usually below 500 cm⁻¹),^{18–21} p is the number of phonons to bridge the ΔE ($p = \Delta E/h\nu_{max}$), and k is the Boltzmann constant (6.958 × 10⁻¹ cm⁻¹·K⁻¹). Accordingly, the MPR rate from ³P₀ to ¹D₂ states at 300 K is approximately 2.35 × 10⁴ s⁻¹, which is slightly slower than the radiative transition rate of ³P₀ luminescence (for example ~9.1 × 10⁴ s⁻¹ in Y₃Al₅O₁₂:Pr³⁺ and 2.7 × 10⁵ s⁻¹ in La₂O₃:Pr³⁺),²² implying that the decrease of ³P₀ intensities in Figure 2d is due to collaborations of two processes: radiative to ³H_j ground states and nonradiative to ¹D₂ intermediate level by MPR. The radiative process seems to have a slightly larger contribution than the MPR process.

Figure S4a gives the normalized f–d emission spectra of Ba(Y_{1-x}Pr_x)₂Si₃O₁₀ ($x = 0.005\text{--}0.05$) under 230 nm excitation at RT. With rising doping concentration, the spectral profile does not significantly change, and its intensity increases gradually to become maximum at $x = 0.03$ as plotted in the inset. On the contrary, concentration-dependent f–f luminescence exhibits a strong change as displayed in Figure 3a. When changing the excitation to the 435 nm ³H₄–³P₂ transition, an analogous phenomenon is observed and shown in Figure S4b. As displayed in Figure S4c, emission intensity from the ³P₀ state increases gradually with rising concentration, while that from the ¹D₂ decreases.

Because the electron population efficiency from the Pr³⁺ 4f5d state to the 4f² excited states remains constant with the increase of Pr³⁺ concentration at a fixed temperature, the results demonstrate different concentration-related luminescence properties of ³P₀ and ¹D₂ states. Figure 3b gives the ¹D₂ luminescence decay in samples with different Pr³⁺ concentrations at RT. The curves deviate from the single exponential gradually with increasing Pr³⁺ concentration. This deviation is mainly caused by the possible CR between Pr³⁺ ions. As previously reported,³ the predominant CR channel for electrons in the ¹D₂ state is ascribed to be [¹D₂, ³H₄]-[¹G₄, ³F₄], and that in ³P₀ is [³P₀, ³H₄]-[¹G₄, ¹G₄], respectively. The small energy mismatch (~12 cm⁻¹) of the former channel results in a quite efficient CR process from the ¹D₂ state.²² As a result, the experimental findings in Figure 3a and Figure S4b were observed. Herein, the Inokuti–Hirayama model²³ is employed to analyze the decay of ¹D₂ luminescence:

$$\ln\left(-\ln\left(\frac{I(t)}{I(0)}\right) - \frac{t}{\tau_0}\right) = B + \frac{3}{s} \cdot \ln(t),$$

$$I(t) = I(0)\exp\left(-\frac{t}{\tau_0} - \frac{4\pi}{3}\Gamma\left(1 - \frac{3}{s}\right) \cdot C_A \cdot (C_{DA}^{(s)})^{3/s} \cdot t^{3/s}\right),$$

$$P_{SA} = \frac{C_{DA}^{(s)}}{R_{SA}^s},$$

where s determines the type of multipolar effect and P_{SA} denotes the ET rate. The physical meanings of other parameters in the equations have been defined elsewhere.²⁴ On the basis of the fitting results, the dominant multipolar mechanism is found to be dipole–dipole interaction, and the kinetic microparameter C_{DA} is about 5.962 × 10⁻⁵¹ m⁶·s⁻¹.

ET in Ce³⁺, Pr³⁺-Codoped BaY₂Si₃O₁₀. ET of Pr³⁺ 4f5d → Ce³⁺ 5d. Figure 4a represents the normalized excitation spectra of Ba(Y_{0.99-x}Ce_{0.01}Pr_x)₂Si₃O₁₀ ($x = 0.005\text{--}0.05$) at RT. The excitation spectrum of Ce³⁺ single-doped sample is given as well for comparison. When monitoring 400 nm Ce³⁺ emission, Pr³⁺ 4f²–4f5d transition bands are observed in the spectra in

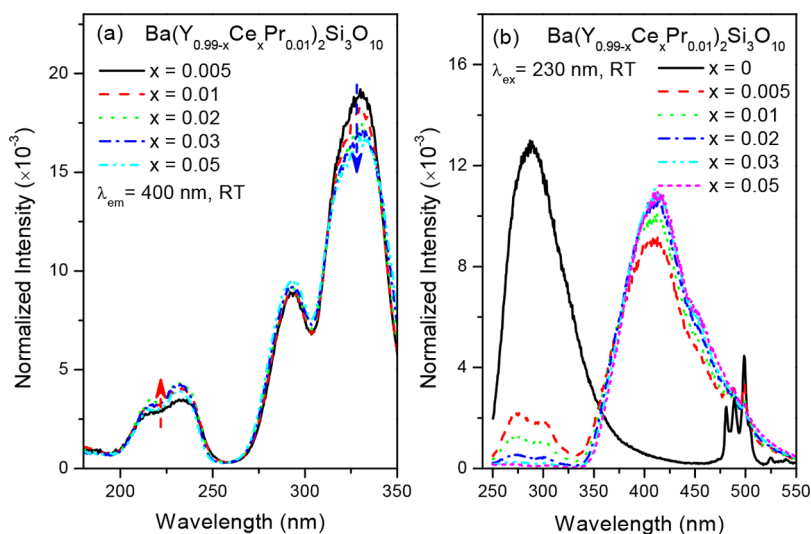


Figure 5. (a) Normalized excitation spectra of $\text{Ba}(\text{Y}_{0.99-x}\text{Ce}_x\text{Pr}_{0.01})_2\text{Si}_3\text{O}_{10}$ ($x = 0.005\text{--}0.05$) samples with 400 nm emission; (b) normalized emission spectra of samples under 230 nm excitation.

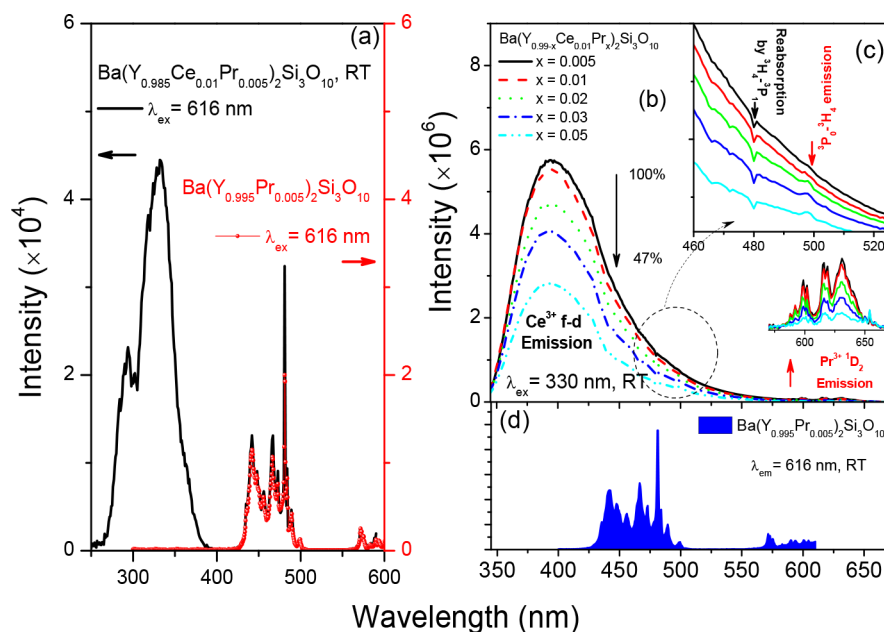


Figure 6. (a) Excitation spectra of $\text{Ba}(\text{Y}_{0.985}\text{Ce}_{0.01}\text{Pr}_{0.005})_2\text{Si}_3\text{O}_{10}$ and $\text{Ba}(\text{Y}_{0.995}\text{Pr}_{0.005})_2\text{Si}_3\text{O}_{10}$ with 616 nm $\text{Pr}^{3+} 1\text{D}_2\text{--}3\text{H}_4$ emission; (b) emission spectra of $\text{Ba}(\text{Y}_{0.99-x}\text{Ce}_{0.01}\text{Pr}_x)_2\text{Si}_3\text{O}_{10}$ ($x = 0.005\text{--}0.05$) under 330 nm excitation at RT; the inset represents the enlargement of $\text{Pr}^{3+} 1\text{D}_2\text{--}3\text{H}_4$ emission; (c) the partial enlargement of spectra b in the 460–525 nm region; (d) excitation spectrum of $\text{Ba}(\text{Y}_{0.985}\text{Pr}_{0.005})_2\text{Si}_3\text{O}_{10}$ with 616 nm emission for comparison.

addition to Ce^{3+} f–d excitations. Considering that no Pr^{3+} emission can be detected at 400 nm, the phenomenon implies that the ET takes place from $\text{Pr}^{3+} 4\text{f}5\text{d}$ to $\text{Ce}^{3+} 5\text{d}$ states. With the increase of Pr^{3+} concentration in $\text{Ba}(\text{Y}_{0.99-x}\text{Ce}_{0.01}\text{Pr}_x)_2\text{Si}_3\text{O}_{10}$, the relative contributions of Pr^{3+} f–d excitation bands in the spectra increase and those of Ce^{3+} excitation bands decrease. Under 230 nm Pr^{3+} f–d excitation, the emission spectra of samples are shown in Figure 4b. The relatively weak Pr^{3+} f–d emission is observed in the high-energy region, and its spectral profile in the codoped sample exhibits a significant change compared with that in Pr^{3+} single-doped sample in Figure 1b. The enlargement (black dots) is displayed in the inset, and two dips at 293 and 330 nm are detected in the spectrum as marked by blue arrows. As displayed in Figure S2, two strong excitation bands are seen in

the excitation spectrum of Ce^{3+} doped sample at about 293 and 330 nm, respectively. It is reasonable to assign the two dips to the absorption of Ce^{3+} because of the spectral overlap between Pr^{3+} f–d emission and Ce^{3+} excitation, confirming the ET from $\text{Pr}^{3+} 4\text{f}5\text{d}$ to $\text{Ce}^{3+} 5\text{d}$ states. With the increase of Pr^{3+} concentration, the intensity of Pr^{3+} f–d emission rises gradually to the maximum at $x = 0.03$. Meanwhile, the strong Ce^{3+} emission is observed, while its intensity decreases stepwise. This may relate to another type of ET from $\text{Ce}^{3+} 5\text{d}$ to $\text{Pr}^{3+} 4\text{f}^2$ states, which will be discussed later.

When rising Ce^{3+} concentration in $\text{Ba}(\text{Y}_{0.99-x}\text{Ce}_x\text{Pr}_{0.01})_2\text{Si}_3\text{O}_{10}$ ($x = 0.005\text{--}0.05$) with a fixed Pr^{3+} doping concentration, the normalized excitation spectra with 400 nm emission are provided in Figure 5a. Like the results in Figure 4a, the relative intensities of Pr^{3+} f–d excitations

increase along with those of Ce^{3+} excitations decreasing gradually as Ce^{3+} concentration rises. Upon 230 nm excitation, the normalized emission spectra of $\text{Ba}(\text{Y}_{0.99-x}\text{Ce}_x\text{Pr}_{0.01})_2\text{Si}_3\text{O}_{10}$ ($x = 0-0.05$) at RT are shown in Figure 5b. In Pr^{3+} single-doped sample ($x = 0$), the spectrum shows only Pr^{3+} f-d and f-f emissions. The incorporation of a very small amount of Ce^{3+} ($x = 0.005$) produces the strong Ce^{3+} luminescence, and further rising Ce^{3+} concentration in samples causes the decrease of Pr^{3+} f-d relative emission intensity and the increase of that of Ce^{3+} . Indeed, $\text{Pr}^{3+} 4f5d \rightarrow \text{Ce}^{3+} 5d$ ET gives rise to the increase in Ce^{3+} emission intensity; the contribution of simultaneous excitation of Ce^{3+} should not be neglected. In $\text{Ba}(\text{Y}_{0.99}\text{Ce}_{0.01})_2\text{Si}_3\text{O}_{10}$, the sample shows the 4f-5d₄ absorption around 230 nm as displayed in Figure 4a. Therefore, besides the possible $\text{Pr}^{3+} \rightarrow \text{Ce}^{3+}$ ET, we consider that Ce^{3+} luminescence in codoped samples can be also obtained under the intrinsic f-d excitation to some extent. Accordingly, the strong Ce^{3+} emissions in codoped samples are the combined results of $\text{Pr}^{3+} 4f5d \rightarrow \text{Ce}^{3+} 5d$ ET and Ce^{3+} intrinsic excitation, and the gradual-enhanced ET leads to the further increase in Ce^{3+} emission when Ce^{3+} concentration rises from 0.005 to 0.05.

ET of $\text{Ce}^{3+} 5d \rightarrow \text{Pr}^{3+} 4f^2$. Figure 6a shows the excitation spectra of $\text{Ba}(\text{Y}_{0.985}\text{Ce}_{0.01}\text{Pr}_{0.005})_2\text{Si}_3\text{O}_{10}$ and $\text{Ba}(\text{Y}_{0.995}\text{Pr}_{0.005})_2\text{Si}_3\text{O}_{10}$ with 616 nm $\text{Pr}^{3+} 1D_2-3H_4$ emission at RT. Besides Pr^{3+} intrinsic f-f excitation lines, intense Ce^{3+} f-d excitations are clearly observed in the spectrum of the codoped sample, implying that ET from the 5d state of Ce^{3+} to the 4f levels of Pr^{3+} occurs. Figure 6b shows the emission spectra of $\text{Ba}(\text{Y}_{0.99-x}\text{Ce}_{0.01}\text{Pr}_x)_2\text{Si}_3\text{O}_{10}$ ($x = 0.005-0.05$) under 330 nm excitation at RT. Emission intensities of Ce^{3+} decrease significantly (from 100% to 47%) with the increase of Pr^{3+} concentration, and gradually weak $\text{Pr}^{3+} 1D_2-3H_4$ emissions are observed as shown in the inset. Figure 6c shows the enlargement of spectra b in the 460–525 nm region. An increasingly strong dip at 480 nm is observed in the spectra, which is caused by $\text{Pr}^{3+} 3H_4-3P_1$ reabsorption because of the clear overlap between Pr^{3+} f-f excitation and Ce^{3+} emission. Moreover, a peak at 498 nm corresponding to $\text{Pr}^{3+} 3P_0-3H_4$ emission is present, and its intensity increases as Pr^{3+} concentration rises. Because Pr^{3+} cannot be excited at 330 nm, the above-mentioned phenomena indicate that $\text{Ce}^{3+} 5d \rightarrow \text{Pr}^{3+} 4f^2$ ET is active in codoped samples. Ce^{3+} luminescence decays in representative $\text{Ba}(\text{Y}_{0.99-x}\text{Ce}_{0.01}\text{Pr}_x)_2\text{Si}_3\text{O}_{10}$ ($x = 0, 0.01, 0.03, \text{ and } 0.05$) samples are plotted in Figure 7. With the increase of Pr^{3+} concentrations, the decay curves deviate gradually from the monoexponential, demonstrating that the ET of $\text{Ce}^{3+} 5d$ state to $\text{Pr}^{3+} 4f^2$ states becomes more efficient. The Inokuti–Hirayama model²³ is applied in analysis of the involved ET mechanism, and the fitting results indicate that the dipole–dipole interaction is the predominant multipolar effect in the system ($s_{\text{Averaged}} \sim 5.75$) and the value of C_{DA} is about $9.97 \times 10^{-47} \text{ m}^6 \text{ s}^{-1}$. As Pr^{3+} concentration rises, the P_{SA} for this $\text{Ce}^{3+} 5d \rightarrow \text{Pr}^{3+} 4f^2$ ET increases from $3.01 \times 10^5 \text{ s}^{-1}$ ($x = 0.01$) to $6.59 \times 10^6 \text{ s}^{-1}$ ($x = 0.05$), resulting in the decrease of Ce^{3+} emission intensity as shown in Figure 6b.

XEL Performance. Figure 8 presents the XEL spectra of representative Ce^{3+} , Pr^{3+} -doped/codoped samples at RT. The BaF_2 powder was measured under the same experimental condition as a reference to obtain the total light yield of our samples. Upon X-ray excitation, BaF_2 possesses the typical self-trapped exciton luminescence around 300 nm. $\text{Ba}(\text{Y}_{0.99}\text{Ce}_{0.01})_2\text{Si}_3\text{O}_{10}$ excited by X-ray presents a broad emission

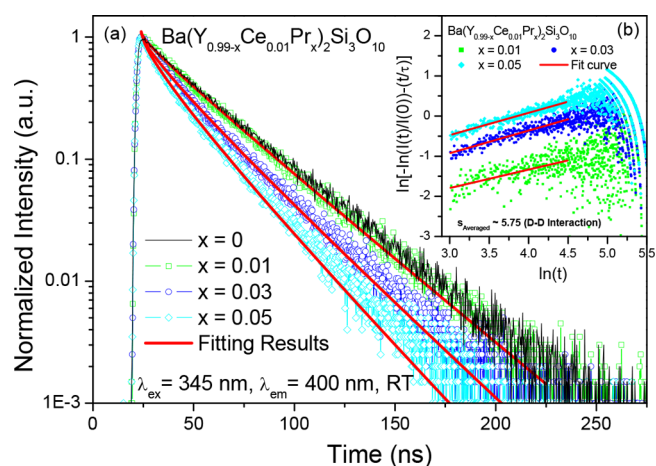


Figure 7. Ce^{3+} luminescence decays in representative $\text{Ba}(\text{Y}_{0.99-x}\text{Ce}_{0.01}\text{Pr}_x)_2\text{Si}_3\text{O}_{10}$ ($x = 0, 0.01, 0.03, \text{ and } 0.05$) samples; the red lines denote the fitting results by the Inokuti–Hirayama model; the inset represents the fitting results of the multipolar mechanism.

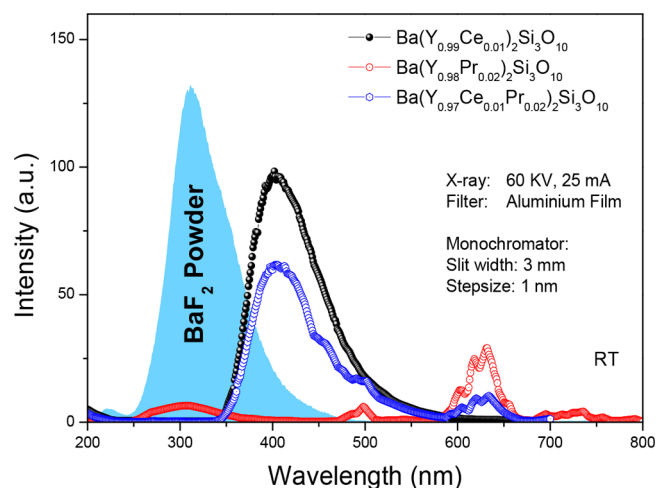


Figure 8. XEL spectra of $\text{Ba}(\text{Y}_{0.99}\text{Ce}_{0.01})_2\text{Si}_3\text{O}_{10}$, $\text{Ba}(\text{Y}_{0.98}\text{Pr}_{0.02})_2\text{Si}_3\text{O}_{10}$, $\text{Ba}(\text{Y}_{0.97}\text{Ce}_{0.01}\text{Pr}_{0.02})_2\text{Si}_3\text{O}_{10}$, and the reference BaF_2 powder at RT.

centered at 400 nm corresponding to Ce^{3+} f-d luminescence. Pr^{3+} f-d and f-f emissions are detected in the spectrum of $\text{Ba}(\text{Y}_{0.98}\text{Pr}_{0.02})_2\text{Si}_3\text{O}_{10}$. $\text{Pr}^{3+} 1D_2-3H_4$ emission becomes predominant in the spectrum upon X-ray excitation, which differs from the spectrum of sample obtained under VUV excitation. It may arise by the different electron population mechanisms because X-ray can excite core electrons to different bound or continuum states, which results in the multiple population pathways returning back to $\text{Ln}^{3+} 4f/5d$ states.^{25,26} Comparing the integrated intensity of the studied samples with that of BaF_2 reference (8880 ph-MeV⁻¹), the total scintillation light yields of $\text{Ba}(\text{Y}_{0.99}\text{Ce}_{0.01})_2\text{Si}_3\text{O}_{10}$, $\text{Ba}(\text{Y}_{0.98}\text{Pr}_{0.02})_2\text{Si}_3\text{O}_{10}$, and $\text{Ba}(\text{Y}_{0.97}\text{Ce}_{0.01}\text{Pr}_{0.02})_2\text{Si}_3\text{O}_{10}$ are approximately 7540, 1690, and 5170 ph-MeV⁻¹, respectively. Due to the relatively low light yield under X-ray excitation, Ce^{3+} -doped $\text{BaY}_2\text{Si}_3\text{O}_{10}$ may be not suitable for the potential scintillator material, and the cosubstitution of Pr^{3+} dissipates Ce^{3+} XEL instead of the improvement, resulting in the decline of scintillation performance of studied materials.

CONCLUSION

Ce³⁺, Pr³⁺-doped BaY₂Si₃O₁₀, prepared by a high temperature solid-state reaction technique, generates attractive optical properties. Pr³⁺ 4f²-4f5d₁₋₃ transition energies are determined in the VUV–UV excitation spectrum, and intense Pr³⁺ 4f5d₁₋₃H₄₋₆ parity-allowed emissions are observed in Ba-(Y_{1-x}Pr_x)₂Si₃O₁₀ samples. Upon 230 nm excitation, the samples also show the 4f–4f emissions, which are mainly the result of electron population from the Pr³⁺ 4f5d state to the next lower-lying 4f excited states through a configuration-coordinate crossover pathway. The TRES technique is employed to determine the ³P₀ and ¹D₂ emission lines in the spectra, and the contribution of MPR on intraconfigurational electron population between Pr³⁺ ³P₀ and ¹D₂ states is discussed. As Pr³⁺ concentration rises, Pr³⁺ ³P₀ and ¹D₂ luminescence possesses different concentration-related properties. Concentration-quenching mechanism of ¹D₂ luminescence is confirmed, and the result indicates that the dominant multipolar mechanism involved is dipole–dipole interaction and the C_{DA} is approximately 5.962 × 10⁻⁵¹ m⁶·s⁻¹.

When monitoring 400 nm Ce³⁺ emission, Pr³⁺ 4f²-4f5d transition bands are clearly observed in the excitation spectra of Ce³⁺, Pr³⁺ codoped samples, and their relative contributions become larger with the increase of Pr³⁺ concentration, demonstrating the more efficient ET in the system. Two visible dips on Pr³⁺ f-d emission profile in the spectra of codoped samples confirm the ET from Pr³⁺ 4f5d to Ce³⁺ 5d states in the system. In addition, the incorporation of Ce³⁺ in the codoped sample produces the strong Ce³⁺ luminescence under 230 nm excitation, which is the combined result of Pr³⁺ 4f5d → Ce³⁺ 5d ET and Ce³⁺ intrinsic excitation. Changing the excitation to 330 nm, the increasingly strong ET of Ce³⁺ 5d → Pr³⁺ 4f² leads to the decrease of Ce³⁺ emission intensity and the gradual deviation of Ce³⁺ luminescence decay. The dipole–dipole interaction is attributed to the predominant multipolar effect in controlling this ET process, and the value of C_{DA} is determined to be 9.97 × 10⁻⁴⁷ m⁶·s⁻¹. Finally, the relatively low scintillation light yield of Ce³⁺-doped BaY₂Si₃O₁₀ impedes its application potential in the scintillator field, and the cosubstitution of Pr³⁺ results in the decline of scintillation performance instead of the improvement as contrary to expectation.

ASSOCIATED CONTENT

Supporting Information

The Supporting Information is available free of charge on the ACS Publications website at DOI: 10.1021/acs.inorgchem.8b01084.

The detailed sample preparation and measurement (SI-PART A), XRD patterns of representative samples (Figure S1), VUV–UV excitation and emission spectra of Ba(Y_{0.999}Ce_{0.001})₂Si₃O₁₀ (Figure S2), decay curve of Pr³⁺ f–d luminescence in Ba(Y_{0.995}Pr_{0.005})₂Si₃O₁₀ (Figure S3), normalized emission spectra of Ba-(Y_{1-x}Pr_x)₂Si₃O₁₀ (x = 0.005–0.05) under different excitations (Figure S4) (PDF)

AUTHOR INFORMATION

Corresponding Author

*E-mail: cesbin@mail.sysu.edu.cn.

ORCID

Rui Shi: 0000-0002-3120-0596

Hongbin Liang: 0000-0002-3972-2049

Notes

The authors declare no competing financial interest.

ACKNOWLEDGMENTS

The work is financially supported by the National Natural Science Foundation of China (U1432249, 21671201, and U1632101), the Science and Technology Project of Guangdong Province (2017A010103034), and the Science and Technology Foundation of Guangzhou City (2016201604030043, 201707010212).

REFERENCES

- (1) Liu, T. C.; Cheng, B. M.; Hu, S. F.; Liu, R. S. Highly Stable Red Oxynitride β-SiAlON: Pr³⁺ Phosphor for Light-Emitting Diodes. *Chem. Mater.* **2011**, *23*, 3698–3705.
- (2) Yen, W. M.; Shionoya, A.; Yamamoto, H. *Phosphor Handbook*, 2nd ed.; CRC Press: Boca Raton, FL, 2007.
- (3) Shi, R.; Lin, L.; Dorenbos, P.; Liang, H. Development of a Potential Optical Thermometric Material through Photoluminescence of Pr³⁺ in La₂MgTiO₆. *J. Mater. Chem. C* **2017**, *5*, 10737–10745.
- (4) Wang, L.; Zhang, X.; Hao, Z.; Luo, Y.; Zhang, J.; Wang, X. J. Interionic Energy Transfer in Y₃Al₅O₁₂:Ce³⁺, Pr³⁺ Phosphor. *J. Appl. Phys.* **2010**, *108*, 093515.
- (5) Schipper, W. J.; Hoogendorp, M. F.; Blasse, G. The Luminescence and X-ray Storage Properties of Pr³⁺ and Ce³⁺ in YNbO₄ and M'-YTaO₄. *J. Alloys Compd.* **1993**, *202*, 283–287.
- (6) Shi, R.; Wang, X.; Huang, Y.; Tao, Y.; Zheng, L.; Liang, H. Site Occupancy and VUV-UV-Vis Photoluminescence of the Lanthanide Ions in BaY₂Si₃O₁₀. *J. Phys. Chem. C* **2018**, *122*, 7421–7431.
- (7) Van Pieterse, L.; Reid, M. F.; Wegh, R. T.; Soverna, S.; Meijerink, A. 4fⁿ→4fⁿ⁻¹5d Transitions of the Light Lanthanides: Experiment and Theory. *Phys. Rev. B: Condens. Matter Mater. Phys.* **2002**, *65*, 045113.
- (8) Dorenbos, P. The 4fⁿ↔4fⁿ⁻¹5d Transitions of the Trivalent Lanthanides in Halogenides and Chalcogenides. *J. Lumin.* **2000**, *91*, 91–106.
- (9) George, N. C.; Birkel, A.; Brgoch, J.; Hong, B. C.; Mikhailovsky, A. A.; Page, K.; Lobet, A.; Seshadri, R. Average and Local Structural Origins of the Optical Properties of the Nitride Phosphor La_{3-x}Ce_xSi₆N₁₁ (0 < x ≤ 3). *Inorg. Chem.* **2013**, *52*, 13730–13741.
- (10) Ning, L.; Lin, L.; Li, L.; Wu, C.; Duan, C.; Zhang, Y.; Seijo, L. Electronic Properties and 4f→5d Transitions in Ce-Doped Lu₂SiO₅: A Theoretical Investigation. *J. Mater. Chem.* **2012**, *22*, 13723–13731.
- (11) Xia, Z.; Miao, S.; Chen, M.; Molokeev, M. S.; Liu, Q. Structure, Crystallographic Sites, and Tunable Luminescence Properties of Eu²⁺ and Ce³⁺/Li⁺-Activated Ca_{1.65}Sr_{0.35}SiO₄ Phosphors. *Inorg. Chem.* **2015**, *54*, 7684–7691.
- (12) Dorenbos, P. Exchange and Crystal Field Effects on the 4fⁿ⁻¹5d Levels of Tb³⁺. *J. Phys.: Condens. Matter* **2003**, *15*, 6249.
- (13) De Mello Donegá, C.; Dirksen, G. J.; Folkerts, H. F.; Meijerink, A.; Blasse, G. The Vibronic Spectroscopy and Luminescence Concentration Quenching of the Pr³⁺ Ion in La₂O₃, LaOF and LiYF₄. *J. Phys. Chem. Solids* **1995**, *56*, 267–276.
- (14) Li, Y.; Wang, J.; Wang, X. M.; Pan, F.; Zhou, T.; Xie, R. J. Colour Tuning via Crystalline Site-Selected Energy Transfer in a Sr₂SiO₄: Eu²⁺, Pr³⁺ Phosphor. *J. Mater. Chem. C* **2017**, *5*, 1022–1026.
- (15) van Dijk, J. M. F.; Schuurmans, M. F. H. On the Nonradiative and Radiative Decay Rates and a Modified Exponential Energy Gap Law for 4f-4f Transitions in Rare-Earth Ions. *J. Chem. Phys.* **1983**, *78*, 5317–5323.
- (16) De Mello Donegá, C.; Meijerink, A.; Blasse, G. Non-Radiative Relaxation Processes of the Pr³⁺ Ion in Solids. *J. Phys. Chem. Solids* **1995**, *56*, 673–685.

- (17) Liu, G.; Jacquier, B. *Spectroscopic Properties of Rare Earths in Optical Materials*, Vol. 83; Springer Science & Business Media: 2006.
- (18) El-Deen, L. S.; Al Salhi, M. S.; Elkholy, M. M. IR and UV Spectral Studies for Rare Earths-Doped Tellurite Glasses. *J. Alloys Compd.* **2008**, *465*, 333–339.
- (19) Zinatloo-Ajabshir, S.; Salavati-Niasari, M. Nanocrystalline Pr₆O₁₁: Synthesis, Characterization, Optical and Photocatalytic Properties. *New J. Chem.* **2015**, *39*, 3948–3955.
- (20) Gouteron, J.; Michel, D.; Lejus, A. M.; Zarembowitch, J. Raman Spectra of Lanthanide Sesquioxide Single Crystals: Correlation between A and B-Type Structures. *J. Solid State Chem.* **1981**, *38*, 288–296.
- (21) Zarembowitch, J.; Gouteron, J.; Lejus, A. M. Raman Spectra of Lanthanide Sesquioxide Single Crystals with A-Type Structure. *Phys. Status Solidi B* **1979**, *94*, 249–256.
- (22) Dornauf, H.; Heber, J. Concentration-Dependent Fluorescence-Quenching in La_{1-x}Pr_xP₅O₁₄. *J. Lumin.* **1980**, *22*, 1–16.
- (23) Inokuti, M.; Hirayama, F. Influence of Energy Transfer by the Exchange Mechanism on Donor Luminescence. *J. Chem. Phys.* **1965**, *43*, 1978–1989.
- (24) Shi, R.; Liu, G.; Liang, H.; Huang, Y.; Tao, Y.; Zhang, J. Consequences of ET and MMCT on Luminescence of Ce³⁺, Eu³⁺, and Tb³⁺-Doped LiYSiO₄. *Inorg. Chem.* **2016**, *55*, 7777–7786.
- (25) Kotani, A. Theory of Core-Level Spectroscopy in f and d Electron Systems. *J. Electron Spectrosc. Relat. Phenom.* **1999**, *100*, 75–104.
- (26) Nikl, M. Energy Transfer Phenomena in the Luminescence of Wide Band-Gap Scintillators. *Phys. Status Solidi A* **2005**, *202*, 201–206.